High-Q Integrated CMOS-MEMS Resonators With Deep-Submicrometer Gaps and Quasi-Linear Frequency Tuning

Wen-Chien Chen, *Student Member, IEEE*, Weileun Fang, *Senior Member, IEEE*, and Sheng-Shian Li, *Member, IEEE*

***Abstract*—Integrated CMOS-MEMS free–free beam resonators using pull-in mechanism to enable deep-submicrometer electrode-to-resonator gap spacing without interference in their mechanical boundary conditions (BCs) have been demonstrated simultaneously with low motional impedance and high Q. The key to attaining high Q relies on a decoupling design between pull-in frames for gap reduction and mechanical BCs of resonators. In addition, the use of metal–SiO_2 composite structures has been proved to greatly benefit the thermal stability of CMOS-MEMS resonators. Furthermore, tuning electrodes underneath pull-in frames were designed to offer "*quasi-linear*" frequency tuning capability where linear relationship between tuning voltage and frequency was achieved. In this paper, CMOS-MEMS free–free beam resonators with gap spacings of 110, 210, and 275 nm, respectively, were tested under direct one-port measurement in vacuum, demonstrating a resonator Q greater than 2000 and a motional impedance as low as 112 kΩ and, at the same time, allowing quasi-linear frequency tuning to achieve a total tuning range of 5000 ppm and a sensitivity of 83.3 ppm/V at 11.5 MHz with *zero dc power consumption*. Such a resonator monolithically integrated with a CMOS amplifier, totally occupying a die area of only 300 μm × 130 μm, was also tested with enhanced performance, benefiting future timing reference and RF synthesizing applications. [2011-0223]**

***Index Terms*—Capacitive transduction, CMOS-MEMS, frequency tuning, micromechanical resonator, monolithic integration, RF-MEMS, temperature compensation.**

I. Introduction

RECENT advances in microscale high-Q resonators that utilize CMOS-MEMS fabrication platforms [1]–[3] with low cost and fast turnaround time to allow monolithic integration with transistor circuits have drawn significant attention in timing reference devices and RF communication systems. With their tiny size, high on-chip integration density, Q's in the thousands, and zero dc power consumption, CMOS-MEMS resonators inherently integrated with analog/digital circuitry are expected to bring revolutionized functionalities not only on conventional electronics but also on integrated microsystems [4].

However, among mainstream CMOS-MEMS resonator platforms, the use of minimum electrode-to-resonator gap spacing for resonators still yields enormous motional impedance of MΩ range, much higher than the standard 50 Ω used in industry, due to the limitation on minimum feature size of current CMOS technology [1]–[3] or post-CMOS process caused by RIE-etched constraint [1]. In order to lower the motional impedance of capacitive resonators, the gap reduction mechanisms, such as the use of electrothermal actuator [5], stress-induced self-assembled actuator [6], and electrostatic pull-in [7], as well as piezoresistive sensing [8], have been demonstrated with motional impedance down to the kΩ range, but at the same time along with adverse issues, for instance, the power consumption of Joule heating and the thermal effects on resonance frequencies in [5], uncertainty of actuation force due to the thermal mismatch of composite structures in [6], low-Q effects caused by nonstationary mechanical boundary conditions (BCs) after pull-in [7], and extra power consumption (i.e., dc current needed) for piezoresistive sensing [8]. The aforementioned approaches provide effective gap reduction, resulting in a workable but not the best option for lowering the motional impedance of CMOS-MEMS resonators.

To address the thermal stability of the capacitively transduced resonators, prior approaches take advantage of active compensation techniques, including Joule heating [9], micro-oven with feedback control [10], [11], and bias voltage correction with control circuits [12], [13]. Both of the Joule-heating and micro-oven techniques consume excessive power while complicated parabolic-type control circuits are necessary for the use of bias voltage tuning. On the other hand, passive temperature compensation techniques, such as the stress-induced frequency compensation [14], [15], composite structures consisting of silicon dioxide [16]–[19], and degenerated doping [20], [21], were demonstrated in recent years. However, the stress-induced frequency tuning necessitates individual support design while both of composite material and degenerated doping approaches suffer from restricted thermal budget of high-temperature process and limited set of usable structural materials. In addition, all of the passive compensation techniques mentioned earlier are not capable of frequency tuning after device fabrication.

Manuscript received July 30, 2011; revised December 21, 2011; accepted January 26, 2012. Date of publication April 3, 2012; date of current version May 28, 2012. This work was supported by the National Science Council (NSC) of Taiwan under Grant NSC-100-2221-E-007-033 and the Toward World-Class University Project. Subject Editor A. Seshia.

W.-C. Chen is with the Department of Power Mechanical Engineering, National Tsing Hua University, Hsinchu 30013, Taiwan (e-mail: d9733814@oz.nthu.edu.tw).

W. Fang and S.-S. Li are with the Department of Power Mechanical Engineering, and also with the Institute of NanoEngineering and MicroSystems, National Tsing Hua University, Hsinchu 30013, Taiwan (e-mail: fang@pme.nthu.edu.tw; ssli@mx.nthu.edu.tw).

Color versions of one or more of the figures in this paper are available online at http://ieeexplore.ieee.org.

Digital Object Identifier 10.1109/JMEMS.2012.2189360

1057-7157/$31.00 © 2012 IEEE

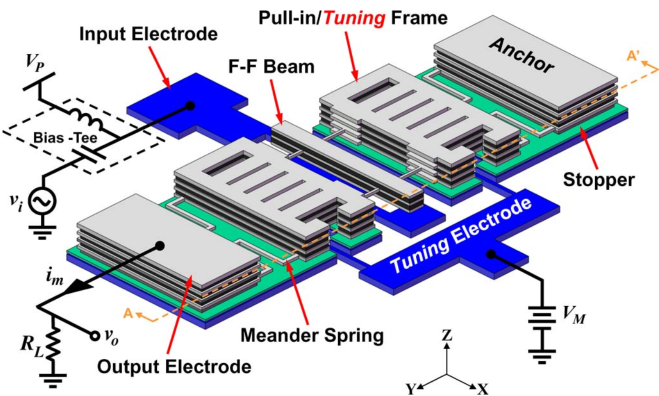

Fig. 1. Perspective-view schematic of a CMOS-MEMS free–free beam resonator with deep-submicrometer gap spacing.

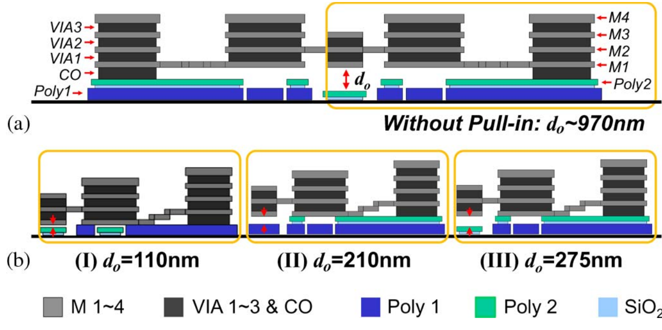

Fig. 2. Side view (A-A′) of the electrode-to-resonator gap configurations of CMOS-MEMS resonators. (a) 970-nm gap before pull-in. (b) Case I: 110-nm gaps, case II: 210-nm gaps, and case III: 275-nm gaps after pull-in.

To overcome the aforementioned issues, this paper details the newly developed CMOS-MEMS free–free beam resonators [22], [23] capable of the following: 1) realizing deep-submicrometer gap spacing to achieve low motional impedance through pull-in mechanism; 2) attaining high Q via free–free beam and mechanical decoupling design which will be described later; 3) improving thermal stability by the use of metal/SiO_2 composite structures; and 4) performing quasi-linear frequency tuning under bias voltage adjustment. After gap reduction via pull-in operation, three deep-submicrometer electrode-to-resonator gaps, including 110, 210, and 275 nm, can be realized, hence leading to motional impedance of fabricated resonators as low as 112 kΩ at a resonance frequency of 11.6 MHz with Q of around 1500. As compared with our previous work [7], the resonator Q value is improved by more than 30$\times$ owing to the decoupling between pull-in frame and mechanical BCs of resonators. In addition, the use of SiO_2 as part of composite structures for resonators brings easy and effective temperature compensation scheme, leading to a linear TC_f of -65 ppm/°C with 5.5$\times$ better than that of mere-metal CMOS-MEMS resonators [3]. With such a limited and *linear* TC_f, CMOS-MEMS composite resonators simply demand a linear frequency tuning mechanism with low cost and low power consumption for temperature compensation. This work has successfully demonstrated quasi-linear frequency tuning via the adjustment of modulated bias voltage without consuming any dc power, showing a 5000-ppm tuning range and a sensitivity of 83.3 ppm/V. In addition, such resonators under frequency tuning operation still preserve steady quality factor Q with very limited influence on motional impedance R_m, hence ensuring stable resonant performance suited for future oscillator and time-keeping applications. Notwithstanding direct measurement capability without the help of amplifier circuitry, on-chip CMOS-MEMS resonators monolithically integrated with CMOS transimpedance amplifiers have also been realized in this work to facilitate the designs and applications of future integrated micromechanical circuits.

II. Gap Reduction and Resonator Design

Fig. 1 shows the perspective view schematic of a CMOS-MEMS resonator along with an appropriate bias, excitation, and sensing configuration. As shown in Fig. 1, a free–free beam resonator is encompassed by a pair of pull-in frames with four tiny supporting beams attached to the nodal locations of the resonator structure. Such tiny supports would substantially eliminate the vibrational energy flow through the path from the supports to the anchored substrate, therefore preserving resonant energy inside the resonator structure and attaining high Q. To lower the required pull-in voltage, the pull-in frames are connected to their adjacent anchors using soft meander springs.

A. Pull-In Induced Gap Reduction and Decoupling Concept

Although our previously designed pinned–pinned beam-array resonators [7] with gap reduction scheme via pull-in have already shown low motional impedance compared to that of other CMOS-MEMS counterparts, they still suffered significant vibration energy loss (i.e., resonator Q's only around 50) and frequency variation due to modulated mechanical BCs. To solve both frequency variation and Q degradation in our previous design [7], a free–free beam with two movable frames indicated in Fig. 1 is designed to simultaneously obtain a stable resonance frequency and high Q. The key to attaining such performance relies on the mechanical decoupling of the pull-in frames and resonator structure where four tiny tethers attached to the nodal locations of the resonator are used to isolate resonator vibration from the influence of pull-in operation, effectively raising resonator Q's up to 2000 and still maintaining relatively steady resonance frequency under different bias voltage V_P.

Before resonator operation, the original electrode-to-resonator gap spacing is around 970 nm which is defined by the thickness of sacrificial oxide in 0.35-μm foundry CMOS process as shown in Fig. 2(a). Such gap spacing leads to considerably high motional impedance and prevents direct measurement using the 50-Ω-based test facility. As a result, gap reduction is crucial for current CMOS-MEMS resonators to achieve reasonable motional impedance. In a normal pull-in operation for gap reduction in Fig. 1, a bias voltage V_M is applied onto the pull-in/tuning electrode (i.e., V_M port) while the input electrode (i.e., V_P port) and resonator structure (i.e., v_o port) are biased at 0 V through bias tees. Such a bias voltage difference (i.e., value of V_M) between pull-in/tuning electrodes (V_M) and movable frames (dc ground) would generate an electrostatic force which intends to pull down the movable frames since the meander springs are designed with very low stiffness.

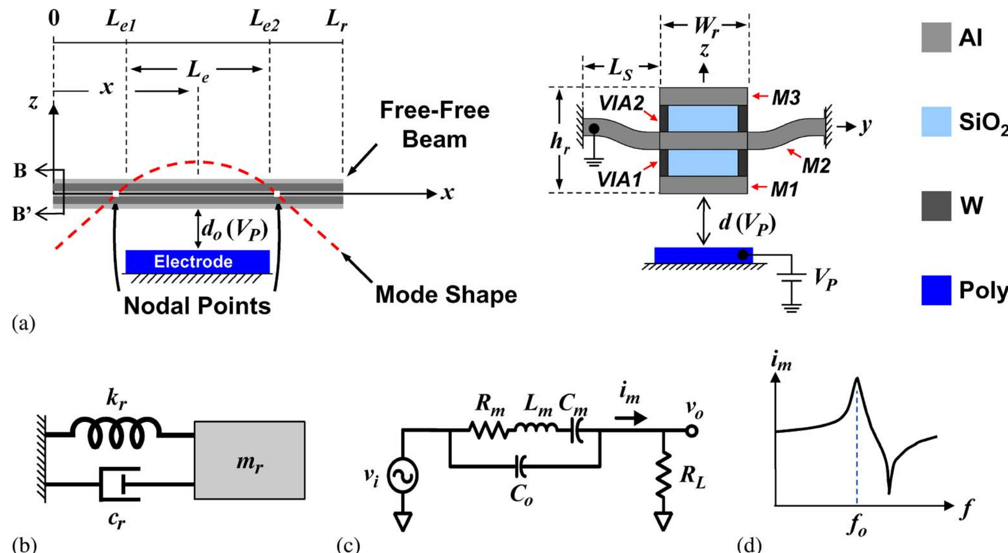

Fig. 3. (a) Resonator side view (x–z plane) and cross-sectional view (B-B′, y–z plane), identifying key parameters for theoretical modeling. (b) Equivalent lumped mechanical circuit. (c) Equivalent RLC circuit. (d) High-Q bandpass biquad behavior for the CMOS-MEMS composite free–free beam resonator.

Once V_M is greater than the pull-in voltage of this mechanical system, the movable frames would then land on the stoppers to enable deep-submicrometer electrode-to-resonator gaps as shown in Fig. 2(b). The pull-in threshold voltage $V_{\text{Pull-in}}$ can be expressed as

$$V_{\text{Pull-in}} = \sqrt{\frac{8}{27}\frac{k_{\text{meander}}\, d_{o,M}^3}{\varepsilon_o A_M}} \tag{1}$$

where k_{meander} is the effective stiffness of the four meander springs, $d_{o,M}$ and A_M are the original gap spacing and overlap area, respectively, between the movable frames and pull-in/tuning electrodes, and ε_o is the permittivity in vacuum. After device pull-in, there are three different deep-submicrometer gap configurations formed by different combinations of the existing CMOS layers (standard Taiwan Semiconductor Manufacturing Company (TSMC) 0.35-μm 2P4M CMOS process), including 110, 210, and 275 nm, respectively, which are determined by the altitude difference between the input electrode and pull-in stoppers as shown in Fig. 2(b). In case (I) of Fig. 2(b), the 110-nm gap configuration is set by the thickness difference between $Poly1$ layer (i.e., frame stopper) and $Poly2 + \text{SiO}_2$ (i.e., input electrode). The 210-nm configuration is defined by the thickness of $Poly2 + \text{SiO}_2$ as shown in case (II) of Fig. 2(b) while the 275-nm configuration is determined by the thickness of $Poly1$ as shown in case (III) of Fig. 2(b).

B. Resonator Operation and Modeling

To excite a CMOS-MEMS composite resonator (shown in Fig. 1 for typical one-port testing configuration and in Fig. 3 for theoretical modeling), an input ac signal v_i applied onto the input electrode together with a dc-bias voltage V_P applied onto the resonator structure would generate an ac-type electrostatic force governed by

$$F_d = V_p \frac{\partial C}{\partial z} v_i \tag{2}$$

where $\partial C/\partial z$ is the change in electrode-to-resonator capacitance per unit displacement of the resonator. To obtain the mechanical resonance frequency of the composite structure in Fig. 3(a), each layer of the composite beam resonator is assumed to have ideal attachment to its adjacent layers. Consequently, the overall mechanical stiffness of the composite beam resonator can be treated as a shunt combination of stiffness in all layers using the Euler–Bernoulli approach, leading to a nominal mechanical resonance frequency of the composite resonator given by

$$f_{\text{nom}} = \frac{1}{2\pi}\sqrt{\frac{k_m(x)}{m_r(x)}} = \frac{1}{2\pi}(\beta_1 L_r)^2 \sqrt{\frac{\sum(E_i I_i)}{\sum(\rho_i A_i)}}\frac{1}{L_r^2} \tag{3}$$

where $k_m(x)$ and $m_r(x)$ are the mechanical stiffness (without electromechanical coupling) and effective mass, respectively, at location x on the beam resonator, L_r is the length of the beam, β_1 represents the frequency parameter of the fundamental mode of the beam with $(\beta_1 L_r)$ equal to 4.73, i represents the corresponding CMOS structural materials (for example, metal, tungsten, and SiO_2), and E, ρ, A, and I are the Young's modulus, density, cross-sectional area, and moment of inertia of each structural layer, respectively. Please note that most of the layers in the composite beam are away from the neutral axis of the beam; therefore, parallel axis theorem should be considered to calculate the effective moment of inertia for these off-axis layers.

For the purposes of oscillator and filter designs, it is convenient to define an equivalent mass–spring–damper mechanical circuit as shown in Fig. 3(b). Referring to Fig. 3(a), the equivalent mass, spring stiffness, damping factor of Fig. 3(b) can be expressed as [24]

$$m_r(x) = \frac{\rho_{\text{eff}} W_r h_r \int_0^{L_r} [Z_{\text{mode}}(x)]^2\, dx}{[Z_{\text{mode}}(x)]^2} \quad \text{where}$$
$$\rho_{\text{eff}} = \frac{\sum(\rho_i A_i)}{\sum A_i} \tag{4}$$

$$k_r(x) = (2\pi f_o)^2 m_r(x) \quad (5)$$

$$c_r(x) = \frac{\sqrt{k_r(x) m_r(x)}}{Q} \quad (6)$$

where ρ_{eff}, W_r, h_r, and Q are the effective density, width, thickness, and quality factor, respectively, of the resonator and where the mode shape function $Z_{\text{mode}}(x)$ [as shown in Fig. 3(a)] is

$$Z_{\text{mod }e}(x) = \cosh(\beta_1 x) + \cos(\beta_1 x) - \xi\left[\sinh(\beta_1 x) + \sin(\beta_1 x)\right] \quad (7)$$

where

$$\xi = \frac{\cosh(\beta_1 L_r) - \cos(\beta_1 L_r)}{\sinh(\beta_1 L_r) - \sin(\beta_1 L_r)}. \quad (8)$$

Nodal points can be obtained by setting (8) to zero and solving for x to allow attachment of the tiny supporting tethers at this location for preserving high Q.

Under excitation of the electrostatic force in (1), the resonator would then vibrate as the frequency of v_i matches the effective resonance frequency f_o (including effects of electromechanical coupling) of the beam, given by [24]

$$f_o = \frac{1}{2\pi}\sqrt{\frac{k_r(x)}{m_r(x)}} = \frac{1}{2\pi}\sqrt{\frac{k_m(x) - k_e(x)}{m_r(x)}} = \frac{1}{2\pi}\sqrt{\frac{k_m(x)}{m_r(x)}}\left[1 - \left\langle\frac{k_e}{k_m}\right\rangle\right]^{\frac{1}{2}} \quad (9)$$

where $k_r(x)$ is the effective stiffness (including electromechanical coupling) at location x on the beam resonator and k_e is the electrical stiffness which can be utilized for frequency tuning as would be described later in Fig. 18. The quantity $\langle k_e/k_m\rangle$ is given by

$$\left\langle\frac{k_e}{k_m}\right\rangle = V_P^2 \frac{\varepsilon_o W_r L_e}{d(V_P)^3}\frac{1}{k_m(x)} \quad (10)$$

where L_e is the length of the input electrode and $d(V_P)$ is the electrode-to-resonator gap spacing of a given resonator under a specific bias voltage V_P. Note that $d(V_P)$ is a bias-dependent gap spacing corresponding to the bending deformation of the tiny supporting tethers under V_P application rather than the gap spacing denoted in Fig. 2(b). The gap spacing can be expressed as

$$d(V_P) = d_o - \frac{1}{2}V_P^2\frac{\varepsilon_o W_r L_e}{d(V_P)^2}\frac{1}{k_s} \quad \text{where } k_s = \frac{48 E_s I_s}{L_s^3} \quad (11)$$

where d_o is the initial electrode-to-resonator gap spacing of a given resonator without the bias voltage V_P, k_s is the stiffness of the four tiny supports connecting the free–free beam and movable frames, and L_s, E_s, and I_s are the length, Young's modulus, and moment of inertia of each tiny support, respectively. In other words, the second term of $d(V_P)$ in (11) represents the static displacement of the resonator toward the underneath electrode, as shown in the right plot of Fig. 3(a), due to the bending deflection of its tiny supports caused by the electrostatic force from V_P. Since $d(V_p)$ appears on both sides of (11) (i.e., implicit function), (11) is best solved by iteration until $d(V_p)$ converges.

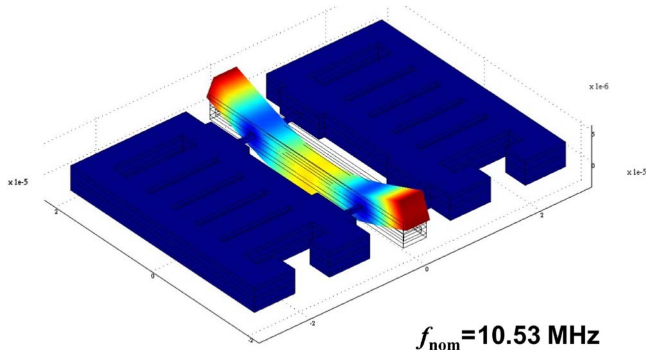

Fig. 4. Finite-element-simulated mode shape for a CMOS-MEMS free–free beam resonator.

At the resonance frequency, the composite beam vibrates into a corresponding mode shape shown in Fig. 4. This motion creates time-varying capacitance between the beam and input electrode, thereby sourcing out an output motional current i_m governed by

$$i_m = V_p\frac{\partial C}{\partial z}\frac{\partial z}{\partial t} \quad (12)$$

where $\partial z/\partial t$ represents the velocity of the resonator. With the use of electromechanical analogy, the vibrating mechanical structure can be modeled as an equivalent RLC circuit shown in Fig. 3(c), where the motional inductance, motional capacitance, and motional impedance are given by the general expressions as

$$L_m = \frac{m_{re}}{\eta_e^2}; \quad C_m = \frac{\eta_e^2}{k_{re}}; \quad R_m = \frac{\sqrt{k_{re} m_{re}}}{Q\eta_e^2} \quad (13)$$

where m_{re} (i.e., $m_r(L_r/2)$) and k_{re} (i.e., $k_r(L_r/2)$) are the effective mass and spring stiffness, respectively, at the center location of the beam and where η_e is the electromechanical coupling coefficient which can be written as [24]

$$\eta_e = V_p\frac{\partial C}{\partial z} = V_p\frac{\varepsilon_o W_r L_e}{d(V_P)^2}. \quad (14)$$

Note that C_o in Fig. 3(c) represents the static capacitance between the input electrode and resonator structure.

In light of the low-loss nature of mechanical vibration, the output motional current i_m versus frequency yields a high-Q bandpass biquad frequency spectrum as shown in Fig. 3(d). All other geometric variables are given in Fig. 3(a).

III. Passive Temperature Compensation and Quasi-Linear Frequency Tuning

Most of micromechanical resonators made by metal are sensitive to temperature variation [3], [25]–[27] due to the negative temperature coefficients of Young's modulus (TC_E's) of their constituent metal materials. To improve the thermal

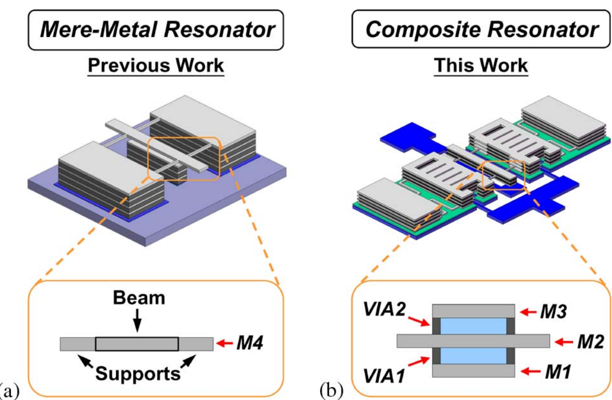

Fig. 5. CMOS-MEMS free–free beam resonators with different structural configurations including (a) a 3.96-MHz mere-metal resonator without temperature compensation and (b) a 11.56-MHz metal–SiO_2 composite resonator with passive temperature compensation capability.

stability of metal-type CMOS-MEMS resonators, the silicon dioxide (SiO_2) in CMOS process with positive TC_E offers a convenient passive temperature compensation scheme where metal–oxide composite structures are utilized to build resonators capable of improving their thermal stability. Furthermore, a voltage-dependent gap modulating mechanism is proposed with an active quasi-linear frequency tuning capability after the device is fabricated (i.e., post frequency tuning ability).

A. Embedded Oxide for Passive Temperature Compensation

In our previous work [3], an out-of-plane free–free beam CMOS-MEMS resonator made by aluminum (i.e., $Metal4$ among CMOS layers) shown in Fig. 5(a) was experimentally characterized with TC_f of -358 ppm/$^\circ$C, much worse than that of silicon-based resonators due to the considerable TC_E of aluminum. To compensate significant frequency drift caused by temperature change for CMOS-MEMS resonators, embedded SiO_2 surrounded by *metal* layers (i.e., $Metal1$ and $Metal3$) and *via* walls (i.e., $VIA1$ and $VIA2$) is utilized to construct composite resonator structures shown in Fig. 5(b) to take advantage of the positive TC_E of SiO_2 for temperature compensation.

The nominal mechanical resonance frequency of the composite beam resonator composed of three structural materials, including metal (i.e., aluminum alloy), tungsten, and oxide, can be expressed as a combination of the resonance frequency of each portion for a given composite beam by an algebraic manipulation of (3) and given by [19]

$$f_{\text{nom}}^2 = \frac{m_{\text{metal}}}{m_r} f_{\text{metal}}^2 + \frac{m_{\text{tungsten}}}{m_r} f_{\text{tungsten}}^2 + \frac{m_{\text{oxide}}}{m_r} f_{\text{oxide}}^2 \quad (15)$$

where m_{metal}, m_{tungsten}, and m_{oxide} are the mass of the constituent metal, tungsten, and oxide, respectively, for a composite beam and f_{metal}, f_{tungsten}, and f_{oxide} are the mechanical resonance frequencies of beams for metal, tungsten, and oxide constituents, respectively. As a result, the linear TC_f of the composite flexural free–free beam resonator can be derived by taking the derivative of (15) with respect to temperature and then simplified as

$$TC_{f1} = \frac{TC_{f1,\text{metal}} + A \cdot TC_{f1,\text{tungsten}} + B \cdot TC_{f1,\text{oxide}}}{1 + A + B} \quad (16)$$

where

$$A = \frac{m_{\text{tungsten}} \cdot f_{\text{tungsten}}^2}{m_{\text{metal}} \cdot f_{\text{metal}}^2} = \frac{E_{\text{tungsten}} \cdot I_{\text{tungsten}}}{E_{\text{metal}} \cdot I_{\text{metal}}} \quad (17)$$

$$B = \frac{m_{\text{oxide}} \cdot f_{\text{oxide}}^2}{m_{\text{metal}} \cdot f_{\text{metal}}^2} = \frac{E_{\text{oxide}} \cdot I_{\text{oxide}}}{E_{\text{metal}} \cdot I_{\text{metal}}} \quad (18)$$

and where $TC_{f1,\text{metal}}$, $TC_{f1,\text{tungsten}}$, and $TC_{f1,\text{oxide}}$ are the linear TC_f's of metal, tungsten, and oxide, respectively; E_{metal}, E_{tungsten}, and E_{oxide} are the Young's moduli of metal, tungsten, and oxide, respectively, and I_{metal}, I_{tungsten}, and I_{oxide} are the moments of inertia of metal, tungsten, and oxide, respectively. In addition, the linear TC_f of each material in (16) can be expressed as [19]

$$TC_{f1,\text{mat}} = \frac{TC_{E1,\text{mat}} + \alpha_{1,\text{mat}}}{2} \quad (19)$$

where $TC_{E1,\text{mat}}$ and $\alpha_{1,\text{mat}}$ are the linear TC_E and the coefficient of thermal expansion (CTE), respectively, of each structural material. In (19), $TC_{E1,\text{mat}}$ is the major parameter to induce the resonance frequency drift as temperature changes (i.e., $TC_{f1,\text{mat}}$), indicating that our proposed embedded oxide with positive TC_E is effective for passive temperature compensation of CMOS-MEMS resonators. To approach the ultimate goal of zero TC_f, the thermal stability of the proposed CMOS-MEMS composite resonators can be further improved by manipulating the ratio A and ratio B in (17) and (18), respectively. As an extreme case when both A and B are close to zero, it represents that the TC_f of such resonator is exactly the same with that of metal-type resonators while structures with A of zero and infinite B belong to oxide-type resonators exhibiting positive TC_f. The proposed composite structure with oxide embedded in Fig. 5(b) would possess lower TC_f than that of the metal-type resonators in Fig. 5(a). Furthermore, the use of composite structures also greatly alleviates the structural deformation caused by residual stress often seen in the CMOS-MEMS devices as would be described later in Fig. 11(a).

B. Voltage-Dependent Quasi-Linear Frequency Tuning

The aforementioned passive frequency compensation is not sufficient for precise timing reference devices with stringent thermal stability requirement; therefore, active frequency tuning capability is needed. Although frequency tuning for the CMOS-MEMS resonators could be attained by modulating V_P as addressed in (9) and (10), the nonlinear frequency modulation as well as large fluctuation in R_m necessitates complicated parabolic-type control circuitry for the use of polarization voltage (V_P) tuning [12], [13].

In contrast, as indicated in (10), the electrical stiffness k_e capable of modulating the resonance frequency is also determined

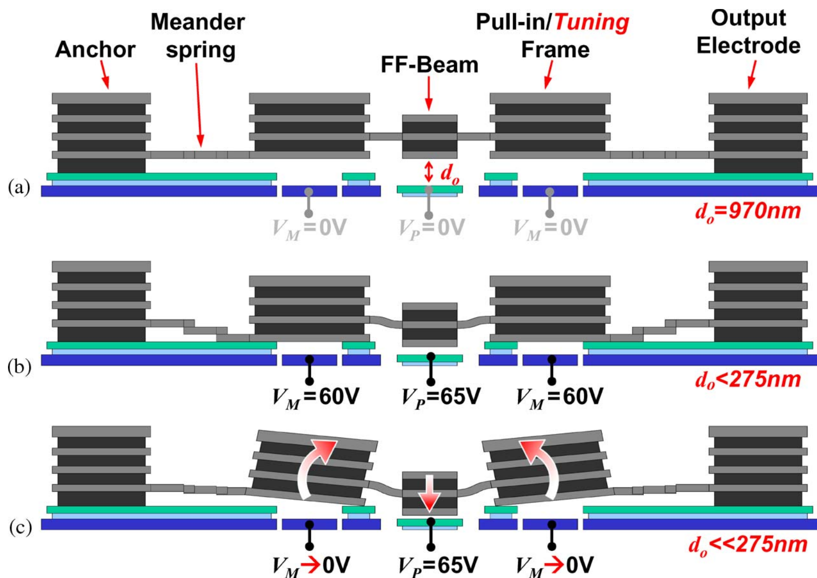

Fig. 6. Side views of the CMOS-MEMS resonator illustrating quasi-linear frequency tuning. (a) Before pull-in. (b) After pull-in. (c) Quasi-linear frequency tuning versus modulated voltage V_M via electrical stiffness.

by electrode-to-resonator gap spacing. Hence, our proposed voltage-dependent gap modulation mechanism for the CMOS-MEMS resonators could provide *quasi-linear* frequency tuning, for the first time, using the adjustment of modulated bias voltage V_M instead of changing V_P, showing much less impact on R_m. To better understand the concept of linear frequency tuning, Fig. 6 shows the structural side view of Fig. 1 to address the physical operation of the CMOS-MEMS free–free beam resonator, including the following: (a) before pull-in operation where $V_P = V_M = 0$ V; (b) after pull-in where $V_P = 65$ V and $V_M = 60$ V; and (c) under adjustment of modulated voltage V_M with fixed device bias V_P. In condition (a), the gap spacing d_o is equal to the contact (CO) thickness of around 970 nm as shown in Fig. 6(a). In condition (b), the pull-in of movable frames occurs when $V_M = 60$ V which is greater than the pull-in threshold voltage $V_{\text{Pull-in}}$ of (1), leading to a d_o of 275 nm as shown in case (III) of Fig. 2(b) (equal to the altitude difference between input electrode and frame stopper [7]). Then, the resonator dc-bias V_P is applied onto the input electrode to further lower the gap spacing to slightly less than 275 nm due to the static deflection of the tiny supporting beams as shown in Fig. 6(b). The BCs of these supporting beams are also shown in the right plot of Fig. 3(a). In condition (c) of the frequency tuning operation, once V_M which is applied onto the tuning electrodes linearly decreases, the resonator body would descend with the pull-in frame rotating into a certain angle to decrease the gap spacing as shown in Fig. 6(c), therefore increasing electrical stiffness k_e and resulting in a downward frequency shift with linear dependence versus V_M.

The mechanical model of electrode-to-resonator gap spacing versus modulated voltage V_M could be simplified as shown in Fig. 7(a). Note that the effect of the meander springs can be eliminated due to their relatively low stiffness, and both free–free beam and pull-in frames could be treated as rigid bodies in static simulation (even with no volume) because of their composite structures. As a result, we could further

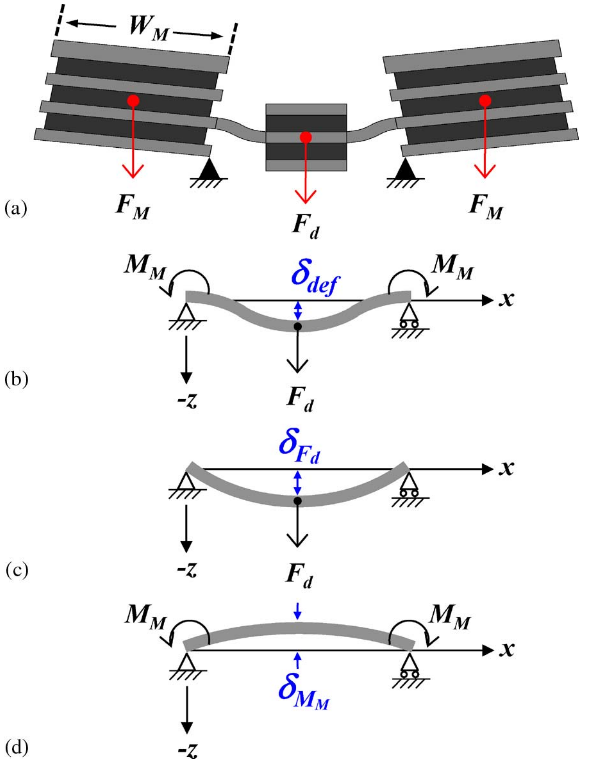

Fig. 7. Mechanical models for CMOS-MEMS free–free beam resonators under gap modulating operation, including the (a) CMOS-MEMS free–free beam resonator with pull-in frames, (b) simplified supporting beam model with simply supported BCs, (c) beam deflection caused by electrostatic force from dc-bias V_P, and (d) deflection which resulted from external moments generated by modulated voltage V_M.

simplify this system into a simply supported beam (i.e., parallel combination of four supporting beams) with overall deflection δ_{def} under external force F_d due to dc-bias V_P and moments M_M generated from the electrostatic force F_M caused by modulated voltage V_M, as shown in Fig. 7(b). Due to the assumption of small deflection, the mechanical system of Fig. 7(b) can

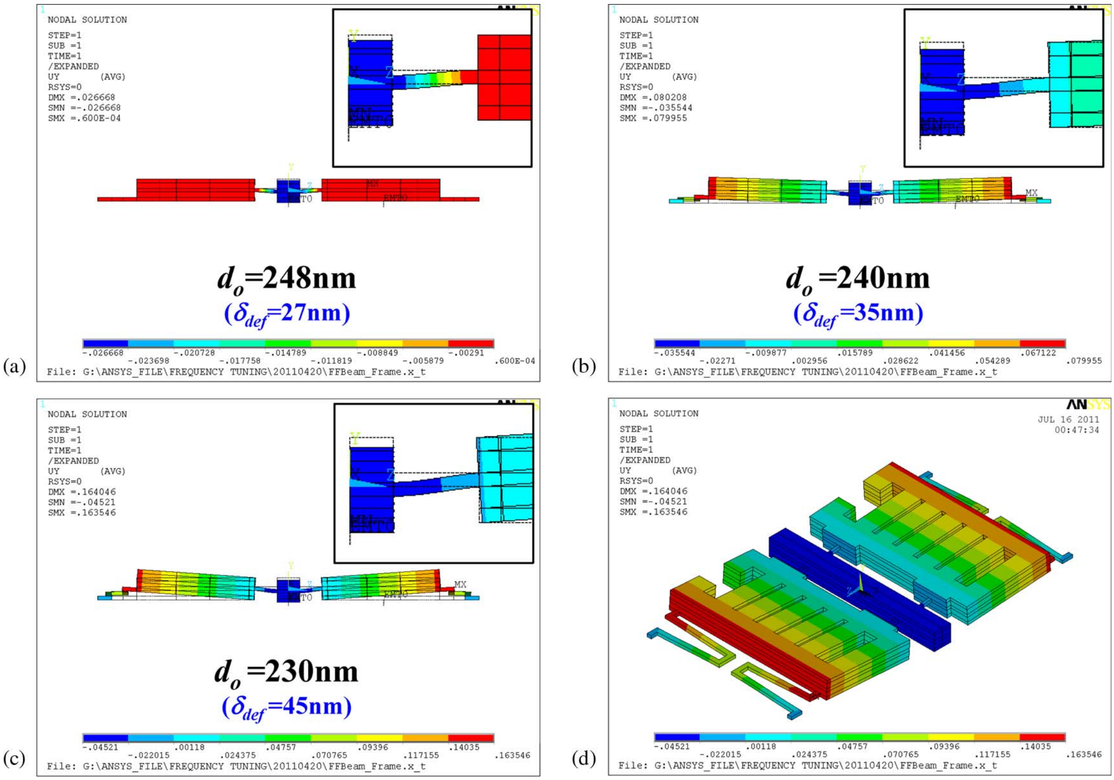

Fig. 8. Finite-element-simulated gap modulation for a CMOS-MEMS free–free beam resonator. (a) After pull-in (V_M is large) but $V_P = 50$ V. (b) $V_P = 50$ V and $V_M = 10$ V. (c) $V_P = 50$ V and $V_M = 0$ V. (d) Global view of 3-D simulated result with the same condition of (c).

be further divided into beam-bending systems of Fig. 7(c) and Fig. 7(d), respectively, for governing equation derivation. Again, the downward beam deflection δ_{Fd} of Fig. 7(c) comes from electrostatic force F_d due to the application of dc-bias V_P while upward beam bending displacement δ_{MM} of Fig. 7(d) is caused by external moments M_M under the application of the modulated voltage V_M. Thus, the total beam deflection $\delta_{\rm def}$ can be derived through the elastic beam theory by summing δ_{Fd} and δ_{MM} together, therefore offering a mechanism to modulate the electrode-to-resonator gap spacing. The gap distance in (11) can be modified as

$$d(V_P, V_M) = d_o - \frac{L_s^3}{24E_sI_s}\left(V_P^2\frac{\varepsilon A_e}{d(V_P, V_M)^2}\right) + \frac{L_s^2}{8E_sI_s}\left(V_M^2\frac{\varepsilon A_M}{d_M(V_P, V_M)^2}W_M\right) \quad (20)$$

where A_e is the electrode-to-resonator overlap area, d_M is the gap spacing between the pull-in frames and modulated electrodes, and W_M is the width of the pull-in frames. It is obvious from (9), (10), and (20) that the final resonance frequency f_o can be tuned by both the device dc-bias voltage V_P and modulated voltage V_M, where the former introduces a nonlinear frequency tuning with significant impacts on R_m while the latter, in contrast, offers a quasi-linear frequency tuning with less effects on R_m. To verify our theoretical modeling, Fig. 8 shows the finite-element simulated results of the static resonator movement under different external loads using a simplified CMOS-MEMS resonator model (i.e., simply supported BC's for pull-in frames without consideration of contact and friction issues which indeed exist in practical modulation operation). In loading condition of Fig. 8(a), the pull-in frames are in full contact with stoppers due to large V_M application while a dc-bias V_P of 50 V is applied onto the resonator structure. The electrostatic force applied onto the resonator is generated by such dc-bias V_P, making the supporting beams deform and leading to 27-nm downward movement of the resonator toward its underneath electrode. The final electrode-to-resonator gap spacing d_o is 248 nm (i.e., 275 nm–27 nm). In the intermediate state of Fig. 8(b), modulated voltage V_M is reduced to 10 V, and the electrostatic force F_M generated by V_M is not sufficient to make full contact between the pull-in frames and stoppers, resulting in overall downward movement of 35 nm for the resonator and leading to a d_o of 240 nm (i.e., 275 nm–35 nm). When V_M is further reduced to 0 V, a minimum d_o of 230 nm is expected due to zero electrostatic force F_M. Fig. 8(d) shows an isoview of ANSYS-simulated deformation for the whole resonator system under the loading condition of Fig. 8(c).

IV. Experimental Results

A. CMOS-MEMS Fabrication Results

To fabricate integrated resonators with deep-submicrometer gaps, a generalized CMOS-MEMS platform [3] using 0.35-μm 2-poly-4-metal CMOS service from TSMC was adopted for device fabrication with a cross-sectional view shown in Fig. 9(a). A maskless post-CMOS release process utilizing commercial SiO_2 etchant, silox vapox III (from Transene Company, Inc.) [3], with very high selectivity between metal and oxide was used to release the resonator structures without the help of

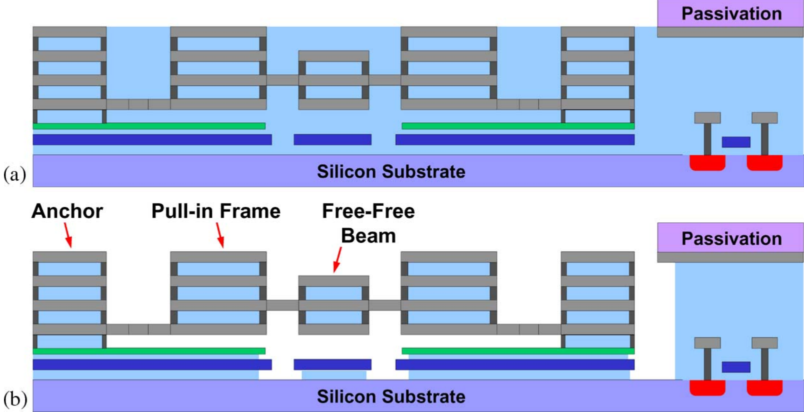

Fig. 9. Cross-sectional views depicting the fabrication process used to achieve integrated CMOS-MEMS resonators in this work. (a) After standard CMOS process. (b) After removal of sacrificial oxide using wet etching (i.e., maskless process).

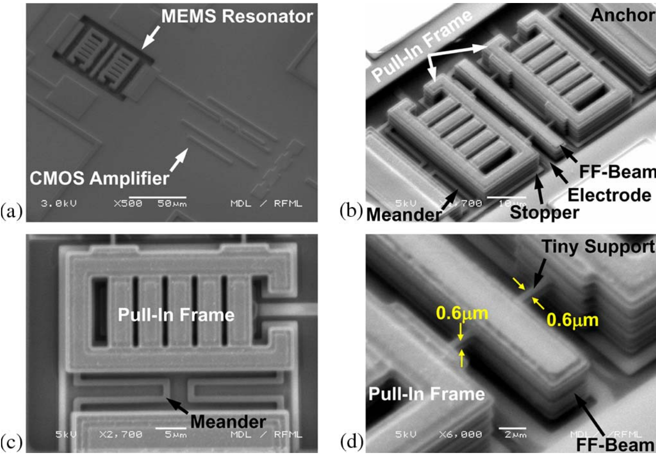

Fig. 10. SEM views of the fabricated CMOS-MEMS resonators. (a) Overall view of CMOS-MEMS integration. (b) Resonator full view. (c) Meander springs connect the pull-in frame and the anchor. (d) Tiny supports of the free–free beam resonator.

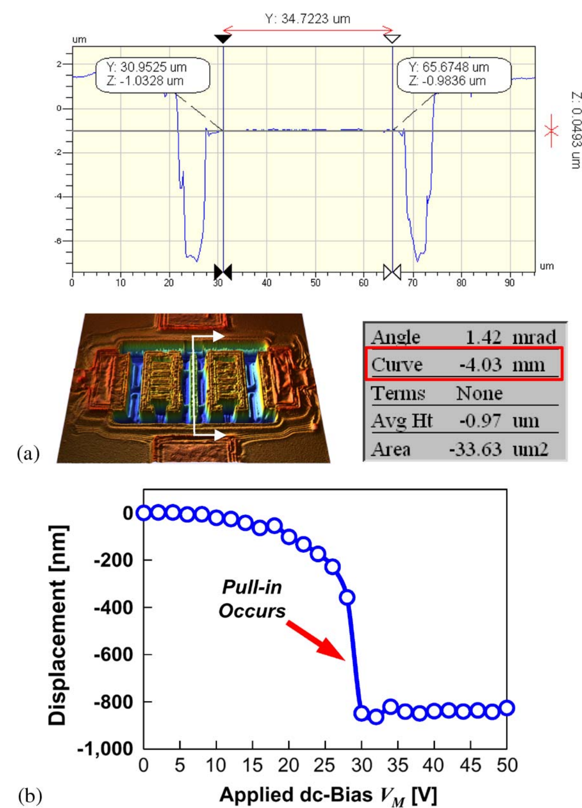

Fig. 11. (a) Radius of curvature caused by residual stress from CMOS layers and (b) pull-in behavior for a fabricated CMOS-MEMS free–free beam resonator.

critical point dryers. After wet release, sacrificial oxide was removed, leaving composite resonator structures, composed of metal and enclosed oxide, free to vibrate while the transistor circuits were protected by the passivation layer as shown in Fig. 9(b). Furthermore, owing to the excellent selectivity of the SiO_2 etchant, the via-connected sidewalls (tungsten) are intact to protect the inner SiO_2 without attacks by the release etchant, hence providing metal/oxide composite which greatly benefits temperature compensation scheme [3], [19] for future timing reference devices since silicon dioxide inherently offers positive temperature coefficient of Young's modulus (TC_E) which is opposite to that of most of the structural materials. Fig. 10 shows the scanning electron microscope (SEM) views of the fabricated CMOS-MEMS composite free–free beam resonators after release process. Fig. 10(a) shows that the MEMS resonator and CMOS amplifier are well connected by metal interconnects, forming a fully integrated CMOS-MEMS circuit. Please note that the CMOS circuitry was indeed protected by the passivation layer during wet release process. Fig. 10(b) further shows that the composite free–free beam resonator is encompassed by the pull-in frames. In Fig. 10(c), the soft mechanical springs formed by slender meander-type beams are designed to lower the pull-in voltage (i.e., at the V_M port of Fig. 1) of the movable frames. Note that the use of these slender supports with width and thickness of only 0.6 μm, clearly seen in Fig. 10(d), is the key to achieving quasi-linear frequency tuning as well as keeping the vibration energy inside the resonator body without leakage to its substrate, thereby preserving high Q.

B. Beam Profile and Pull-In Measurement

The issue of stress gradients on CMOS layers leads to structural bending or curving after release and therefore often impedes the applications of CMOS-MEMS devices. To investigate the residual stress of the fabricated CMOS-MEMS

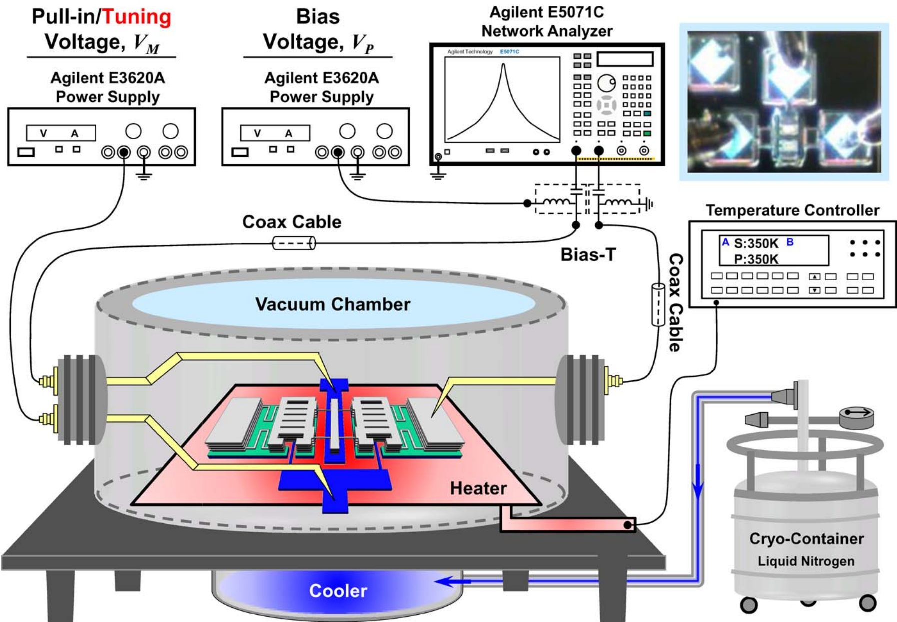

Fig. 12. Schematic illustrating the measurement scheme, showing detailed connections for measurement instrumentation.

free–free beam resonators, Fig. 11(a) shows the surface profile measurement of a fabricated free–free beam by the use of WYKO NT1100 optical profiler, showing a radius of curvature of -4 mm for the composite beam structure in Fig. 10(b). Note that a 0.62-mm radius of curvature was also measured for mere-metal structures [3]. Such an investigation reveals that the stress issue of CMOS-MEMS devices is greatly relieved once the composite structure is used. Fig. 11(b) shows the pull-in behavior of a fabricated CMOS-MEMS composite free–free beam resonator, with the 110-nm gap configuration of case (I) in Fig. 2(b), measured by a white light interferometer, showing that the moving displacement of the resonator is around 860 nm when pull-in occurred at a bias V_M of 28 V. Such pull-in displacement apparently narrows the gap spacing from the original 970 nm down to 110 nm.

C. Measured Spectra for Resonators With Deep-Submicrometer Gaps

A one-port test setup [24], [28] used in this work is shown in Fig. 12 where a cryogenic vacuum probe station providing a pressure level of 20 μtorr is utilized to perform measurement of temperature stability from -40 °C to 80 °C for CMOS-MEMS resonators. Among test facilities, the pull-in bias V_M is connected to the pull-in electrode for gap reduction as well as gap modulation. Through a bias tee, the RF-Out port of an Agilent E5071C network analyzer is connected to the input electrode of the resonator inside the vacuum chamber while the analyzer's RF-In port is linked to the output electrode of the resonator. The dc-bias voltage V_P is applied through the bias tee and then combined with input ac voltage v_i of the RF-Out port onto the input electrode of the resonator.

With a standard short-load-open-through (SLOT) calibration to remove parasitics from the cables and bias tees, Fig. 13(a) and (b) show direct measured frequency characteristics without amplifier circuits for a pinned–pinned beam-array resonator

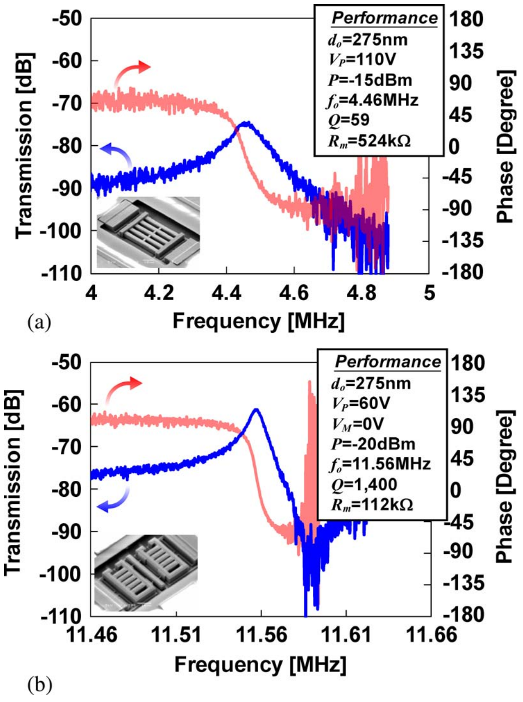

Fig. 13. Measured frequency characteristics of (a) fabricated pinned–pinned beam-array resonator [7] (previous work) and (b) free–free beam resonator (this work).

(i.e., previous design) and single free–free beam resonator (i.e., this work), respectively. As shown, this work only utilized a dc-bias V_P of 60 V, much lower than that of the previous pinned–pinned beam-array design, but achieved resonator Q of 1500 and an R_m of 112 kΩ which are 25 times higher and 4.7 times lower than the pinned–pinned beam-array counterparts, respectively. Please note that the single free–free beam in this work has better performance than that of the array approach in the previous design, indicating that the motional impedance of this work will be further reduced once the array approach is used.

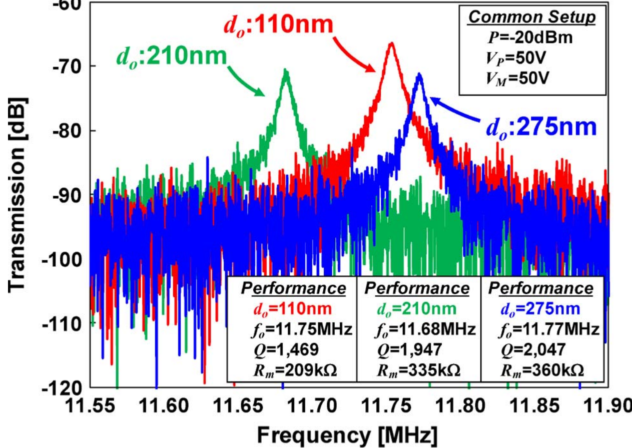

Fig. 14. Measured frequency characteristics of fabricated CMOS-MEMS resonators with different electrode-to-resonator gaps.

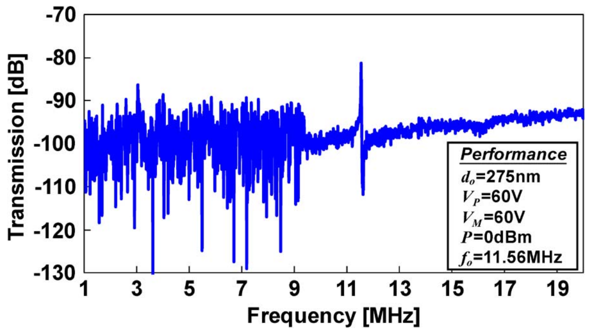

Fig. 15. Wide-span measured spectrum of a fabricated CMOS-MEMS free–free beam resonator, showing only a desired resonance peak without other spurious modes below 20 MHz.

Fig. 14 shows the directly measured spectra without CMOS circuits for the fabricated free–free beam resonators with 110-, 210-, and 275-nm gap configurations of Fig. 2, verifying that smaller gaps lead to lower motional impedance. In order to characterize purely motional performance of resonators in different gap spacings as well as their tuning capability without affection from feedthrough signals, a standard SLOT calibration together with an additional "isolation" provided by the network analyzer was utilized here to remove static capacitance C_O formed by the input electrode and resonator structure, therefore leaving only motional characteristics (i.e., only L_m, C_m, and R_m) and finally resulting in symmetric high-Q biquad frequency response without antiresonance behavior. The measured motional impedances of resonators for 110-, 210-, and 275-nm gap configurations are 209, 335, and 360 kΩ, respectively, at the dc-bias V_P of 50 V and modulated bias V_M of 50 V. Please note that the improvement of motional impedance does not agree well with the reduction of our designed gaps due to postrelease residues between the pull-in frames and stoppers, hence preventing the realization of ideal gaps and leading to higher motional impedances. Fig. 15 further shows the wide-span measured spectrum ranging between 1 and 20 MHz for a fabricated free–free beam resonator, showing that there is no spurious mode existing except the desired resonance peak at 11.56 MHz and also indicating that such a design is well suited for integrated CMOS-MEMS oscillator implementation in the future.

Table I summarizes the design parameters, theoretical modeling, finite-element simulation, and measurement results of the CMOS-MEMS resonators, including out-of-plane free–free beam (Al/W/SiO_2 composite structure) with pull-in gap reduction in this work, in-plane free–free beam (Al/W/SiO_2 composite structure) [3], and out-of-plane mere-metal free–free beam resonators [3]. With the help of gap reduction mechanism, resonators in this work achieve the record low motional impedance R_m while maintaining high Q in high-frequency range among their CMOS-MEMS resonator counterparts.

D. Passive Temperature Compensation Results

Fig. 16 shows the comparison of fractional frequency change versus temperature measurements for an 11.56-MHz metal–SiO_2 composite free–free beam resonator of Fig. 5(b) in this work and a 3.96-MHz mere-metal free–free beam resonator of Fig. 5(a) [3]. Both of the tested resonators are 40 μm long and 4 μm wide but with different thicknesses. The former composed of three metal layers and two enclosed SiO_2 layers, as shown in Fig. 3(a), exhibits a linear TC_f of only -64.83 ppm/°C while the latter made by top aluminum layer of CMOS interconnect metals [3] shows a much worse TC_f of -358 ppm/°C. As a well-known technique, silicon dioxide which provides a positive temperature coefficient of Young's modulus ($TC_E \sim +183$ ppm/°C) in contrast to negative TC_E's of most of MEMS structural materials is often used to perform first-order temperature compensation for resonators [19]. In this paper, enclosed SiO_2 offers a convenient temperature compensation scheme for composite CMOS-MEMS resonators with 5.5× improvement of thermal stability as compared to mere-metal resonators. The composite structures using such a simple temperature compensation scheme effectively lower the fractional frequency variation down to 8000 ppm over temperature range from -40 °C to 80 °C, thereby allowing the application of the proposed quasi-linear frequency tuning to further compensate the remaining frequency drift.

E. Active Frequency Tuning Results

Fig. 17(a) shows the quasi-linear frequency tuning using the adjustment of V_M from 60 to 0 V with a stepped decrement of 4 V, showing that the measured frequency characteristics are very similar except for the total transmission loss of 4.73 dB, equivalent to a 1.72× decrease of R_m. Such limited decrease of R_m is not an issue for oscillator applications when automatic level control is utilized. Fig. 17(b) shows the measured frequency versus V_M, showing a total tuning range of 56.5 kHz and a tuning sensitivity of 0.94 kHz/V at 11.5 MHz. Please note that the tested resonator under different V_M still preserves similar quality factor Q of around 1500, offering a stable performance for future oscillator applications. Fig. 18(a) shows the comparison of frequency tuning approaches using quasi-linear V_M-dependent (tuning range of 5000 ppm and tuning sensitivity of 83.3 ppm/V) and nonlinear V_P-dependent (tuning range of 9000 ppm) mechanisms, indicating that the

TABLE I
CMOS-MEMS RESONATOR DESIGN AND PERFORMANCE SUMMARY

	Structure Design	Deep-Subμ Composite FF-Beam - This Work	Via-Supported Composite FF-Beam [3]	Mere-Metal FF-Beam [3]	Unit
Resonator Type	Resonator SEM				—
Simulated Parameters	μResonator Dimensions, L_r, W_r, h_r	40, 4, 3.945	40, 4, 3.945	40, 4, 0.925	μm
	Electrode Length, L_e	20	19.4	20	μm
	Electrode-to-Resonator Gap, d_o	d_o=0.275[a] (d_o=0.207[b])	0.5	1.0	μm
	dc-Bias Voltage, V_P	60	70	60	V
	Young's Modulus, E_{Al}, E_{SiO2}, E_W	70, 70, 411	70, 70, 411	70, —, —	GPa
	Density, ρ_{Al}, ρ_{SiO2}, ρ_W	2700, 2200, 19350	2700, 2200, 19350	2700, —, —	kg/m^3
	Equivalent Density, ρ_r	4620	4620	2700	kg/m^3
Measured Results	Measured Resonance Frequency, $f_{,meas.}$	11.56	14.53	3.64	MHz
	Motional Impedance, R_m	0.237[b] (min:0.112[c])	5.26	8.22	MΩ
	Measured Quality Factor, Q	1,400	1,590	911	—
Calculated and Simulated Results	Calculated Resonance Frequency, f_{nom}	11.504	15.585	3.026	MHz
	FEM-Simulated Resonance Frequency, f_{nom}	10.53	14.70	3.807	MHz
	Effective Mass, m_{re}	1.97×10^{-12}	1.97×10^{-12}	2.70×10^{-13}	kg
	Mechanical Stiffness, k_m	1.03×10^{4}	1.89×10^{4}	97.79	N/m
	Calculated Resonance Frequency, f_o	11.344	15.579	3.00	MHz
	Effective Stiffness, k_{re}	1.00×10^{4}	1.89×10^{4}	96.30	N/m
	Motional Inductance, L_m	2.02	103.61	287	H
	Motional Impedance, R_m	0.105	6.38	6.00	MΩ
	Motional Capacitance, C_m	0.097	0.001	0.00978	fF
	Static Capacitance, C_o	3.41	1.36	0.71	fF
	Electromechanical Coefficient, η_e	9.88×10^{-7}	1.38×10^{-7}	3.07×10^{-8}	C/m

[a]Indicate gap spacing under gap-reduction operation (V_M = 60V) while dc-bias V_P is not applied (cf. Fig. 6(a)).
[b]Indicate calculation values (via Eq.(11)) under gap-reduction operation (V_M = 60V) while dc-bias V_P is applied (cf. Fig. 6(b)).
[c]Indicate measured R_m under gap-reduction operation while dc-bias V_P was applied and V_M was removed (cf. Fig. 6(c)).

V_M-dependent frequency tuning is much preferred in terms of circuit implementation and practical application for temperature compensation. Furthermore, Fig. 18(b) shows the comparison of motional impedance R_m affected by V_P and V_M, showing that V_M-dependent frequency tuning provides more stable motional output signal.

F. Integrated CMOS-MEMS Circuits

Notwithstanding that the stand-alone CMOS-MEMS resonators with low enough motional impedance allow direct measurement without the need of amplifier circuitry, on-chip CMOS-MEMS resonators monolithically integrated with CMOS transimpedance amplifiers have also been demonstrated in this work as shown in Fig. 19(a) to facilitate the design of future integrated micromechanical circuits. Fig. 19(b) finally shows the measured spectrum of an on-chip CMOS-MEMS resonator integrated with its CMOS trans-impedance amplifier in comparison with a stand-alone resonator, showing that the transmission is greatly improved.

V. CONCLUSION

To lower the motional impedance of CMOS-MEMS resonators, the pull-in mechanism is adopted to surmount the limitation of minimum feature size from the CMOS process and hence to achieve deep-submicrometer electrode-to-resonator gap spacing. A bias-voltage decoupling for pull-in and device operation provides an effective way to attain a steady resonance frequency without the influence of modulated BCs observed

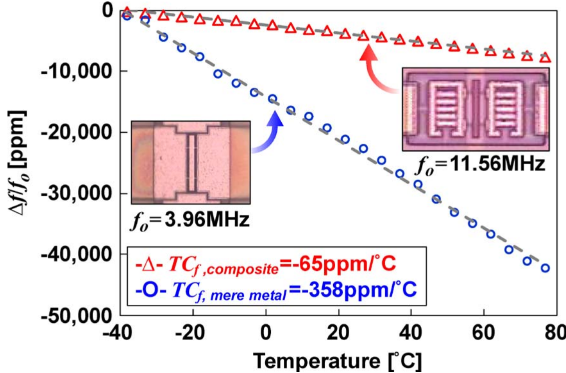

Fig. 16. Measured fractional frequency change versus temperature for 11.56-MHz metal–SiO_2 composite and 3.96-MHz mere-metal free–free beam resonators, demonstrating significant temperature compensation using SiO_2.

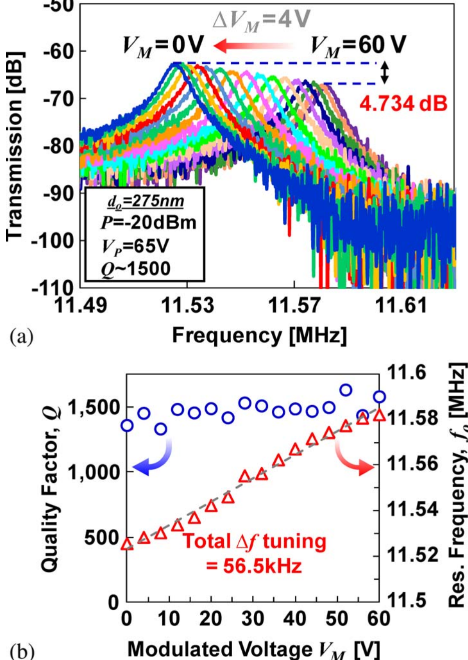

Fig. 17. Measured frequency characteristics for a CMOS-MEMS free–free beam resonator. (a) Measured frequency spectra versus modulated voltage V_M. (b) Quasi-linear frequency tuning versus modulated voltage V_M with invariant quality factor Q.

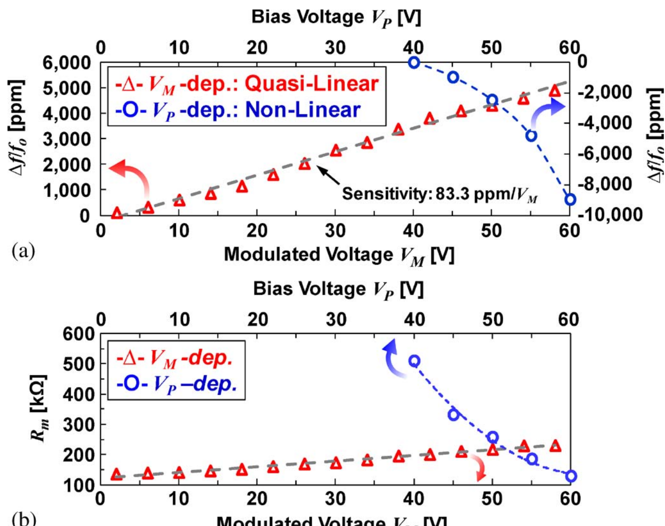

Fig. 18. Comparison between the V_M-dependent and the V_P-dependent frequency tuning for a fabricated CMOS-MEMS free–free beam resonator. (a) Quasi-linear and nonlinear frequency tuning versus bias voltages. (b) Impacts on motional impedance due to the adjustment of bias voltages.

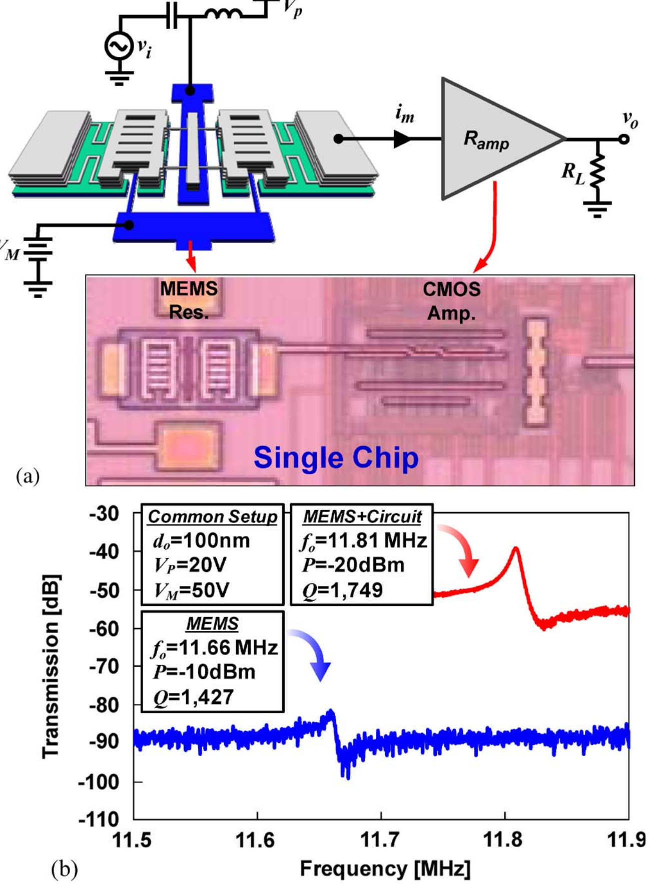

Fig. 19. Fully integrated CMOS-MEMS free–free beam resonator. (a) Measurement scheme with optical photograph. (b) Measured frequency spectra for a stand-alone MEMS resonator and a resonator integrated with its associated CMOS amplifier circuit.

in our previous pinned–pinned beam design. A free–free beam design is also used to reduce the support loss and attain high Q. Therefore, high-Q integrated CMOS-MEMS resonators with deep-submicrometer electrode-to-resonator gap spacing have been demonstrated in this work with motional impedance down to 112 kΩ and with Q's up to 2000 using a single-beam design. It is expected that the motional impedance can be further improved by using array approach, hence greatly benefiting the oscillator applications.

A voltage-dependent quasi-linear frequency tuning for CMOS-MEMS resonators has also been demonstrated in this work using gap-modulated electrical stiffness combined with an elegant mechanical design to benefit temperature compensation of future oscillator and timing reference applications. To limit the frequency variation to less than 1% over 120 °C temperature range (from -40 °C to 80 °C), a metal–oxide composite structure for CMOS-MEMS resonators is used to improve thermal stability via the use of silicon dioxide which possesses positive TC_E, hence achieving $5.5\times TC_f$ improvement compared to

that of mere-metal resonators. With such limited frequency variation (only 8000 ppm), the proposed *quasi-linear* frequency tuning achieves a total tuning range of 5000 ppm with a tuning sensitivity of 83.3 ppm/V, potentially capable of providing temperature compensation for CMOS-MEMS resonators over most of the temperature range. Finally, CMOS-MEMS resonators monolithically integrated with amplifier circuits, occupying die area of only 300 μm $\times$ 130 μm, have been demonstrated with performance enhancement, miniaturization, and integration for future consumer electronics.

Acknowledgment

The authors would like to thank the TSMC and National Chip Implementation Center, Taiwan, for supporting the IC manufacturing.

References

[1] F. Chen, J. Brotz, U. Arslan, C.-C. Lo, T. Mukherjee, and G. K. Fedder, "CMOS-MEMS resonant RF mixer-filters," in *18th IEEE Int. MEMS Conf. Tech. Dig.*, Miami Beach, FL, Jan. 30–Feb. 3, 2005, pp. 24–27.

[2] J. L. Lopez, J. Verd, J. Teva, G. Murillo, J. Giner, F. Torres, A. Uranga, G. Abadal, and N. Barniol, "Integration of RF-MEMS resonators on submicrometric commercial CMOS technologies," *J. Micromech. Microeng.*, vol. 19, no. 1, pp. 13–22, Jan. 2009.

[3] W.-C. Chen, W. Fang, and S.-S. Li, "A generalized CMOS-MEMS platform for micromechanical resonators monolithically integrated with circuits," *J. Micromech. Microeng.*, vol. 21, no. 6, p. 065012, Jun. 2011.

[4] K. D. Wise, "Wireless integrated microsystems: Wearable and implantable devices for improved health care," in *15th Int. Conf. Solid-State Sens. Actuators Tech. Dig., TRANSDUCERS*, Denver, CO, Jun. 21–25, 2009, pp. 1–8.

[5] C.-C. Lo, F. Chen, and G. K. Fedder, "Integrated HF CMOS-MEMS square-frame resonators with on-chip electronics and electrothermal narrow gap mechanism," in *13th Int. Conf. Solid-State Sens. Actuators Tech. Dig., TRANSDUCERS*, Seoul, Korea, Jun. 5–9, 2005, pp. 2074–2077.

[6] G. K. Fedder, "CMOS-MEMS resonators mixer-filters," in *IEEE Int. Electron Devices Mtg. Tech. Dig.*, Washington, DC, Dec. 5, 2005, pp. 274–277.

[7] W.-C. Chen, M.-H. Li, W. Fang, and S.-S. Li, "Realizing deep-submicron gap spacing for CMOS-MEMS resonators with frequency tuning capability via modulated boundary conditions," in *23rd IEEE Int. MEMS Conf. Tech. Dig.*, Hong Kong, Jan. 24–28, 2010, pp. 735–738.

[8] M. K. Zalalutdinov, J. D. Cross, J. W. Baldwin, B. R. Ilic, W. Zhou, B. H. Houston, and J. M. Parpia, "CMOS-integrated RF MEMS resonators," *J. Microelectromech. Syst.*, vol. 19, no. 4, pp. 807–815, Aug. 2010.

[9] M. Hopcroft, R. Melamud, R. N. Candler, W.-T. Park, B. Kim, G. Yama, A. Partridge, M. Lutz, and T. W. Kenny, "Active temperature compensation for micromachined resonators," in *Hilton Head Workshop Tech. Dig.*, Hilton Head Island, SC, Jun. 6–10, 2004, pp. 364–367.

[10] C. M. Jha, M. A. Hopcroft, S. A. Chandorkar, J. C. Salvia, M. Agarwal, R. N. Candler, R. Melamud, B. Kim, and T. W. Kenny, "Thermal isolation of encapsulated MEMS resonators," *J. Microelectromech. Syst.*, vol. 17, no. 1, pp. 175–184, Feb. 2008.

[11] J. C. Salvia, R. Melamud, S. A. Chandorkar, S. F. Lord, and T. W. Kenny, "Real-time temperature compensation of MEMS oscillators using an integrated micro-oven and a phase lock loop," *J. Microelectromech. Syst.*, vol. 19, no. 1, pp. 192–201, Feb. 2010.

[12] G. K. Ho, K. Sundaresan, S. Pourkamali, and F. Ayazi, "Micromechanical IBARs tunable high-Q resonators for temperature-compensated reference oscillator," *J. Microelectromech. Syst.*, vol. 19, no. 3, pp. 503–515, Jun. 2010.

[13] K. Sundaresan, G. K. Ho, S. Pourkamali, and F. Ayazi, "Electronically temperature compensated silicon bulk acoustic resonator reference oscillator," *IEEE J. Solid-State Circuits*, vol. 42, no. 6, pp. 1425–1434, Jun. 2007.

[14] W.-T. Hsu and C. T.-C. Nguyen, "Geometric stress compensation for enhanced thermal stability in micromechanical resonators," in *IEEE Ultrason. Symp. Tech. Dig.*, Sendai, Japan, Oct. 5–8, 1998, pp. 945–948.

[15] W.-T. Hsu, J. R. Clark, and C. T.-C. Nguyen, "Mechanically temperature-compensated flexural-mode micromechanical resonators," in *IEEE Int. Electron Devices Mtg. Tech. Dig.*, San Francisco, CA, Dec. 11–13, 2000, pp. 399–402.

[16] K. M. Lakin, K. T. McCarron, and J. F. McDonald, "Temperature compensated bulk acoustic thin film resonators," in *IEEE Ultrason. Symp. Tech. Dig.*, San Juan, Puerto Rico, Oct. 22–25, 2000, pp. 855–858.

[17] B. Kim, R. Melamud, M. A. Hopcroft, S. A. Chandorkar, G. Bahl, M. Messana, R. N. Candler, G. Yama, and T. W. Kenny, "Si-SiO_2 composite MEMS resonators in CMOS compatible wafer-scale thin-film encapsulation," in *Proc. IEEE Int. Freq. Control Symp.*, Geneva, Switzerland, May 29–Jun. 1, 2007, pp. 1214–1219.

[18] R. Melamud, B. Kim, S. Chandorkar, M. Hopcroft, M. Agarwal, C. Jha, and T. Kenny, "Temperature-compensated high-stability silicon resonators," *Appl. Phys. Lett.*, vol. 90, no. 24, pp. 244107-1–244107-3, Jun. 2007.

[19] R. Melamud, S. A. Chandorkar, B. Kim, H. K. Lee, J. C. Salvia, G. Bahl, M. A. Hopcroft, and T. W. Kenny, "Temperature-insensitive composite micromechanical resonators," *J. Microelectromech. Syst.*, vol. 18, no. 6, pp. 1409–1419, Dec. 2009.

[20] A. K. Samarao and F. Ayazi, "Temperature compensation of silicon micromechanical resonators via degenerate doping," in *IEEE Int. Electron Devices Mtg. Tech. Dig.*, Baltimore, MD, Dec. 7–9, 2009, pp. 1–4.

[21] A. K. Samarao, G. Casinovi, and F. Ayazi, "Passive TCF compensation in high Q silicon micromechanical resonators," in *23rd IEEE Int. MEMS Conf. Tech. Dig.*, Hong Kong, Jan. 24–28, 2010, pp. 116–119.

[22] W.-C. Chen, M.-H. Li, W. Fang, and S.-S. Li, "High-Q integrated CMOS-MEMS resonators with deep-submicron gaps," in *Proc. IEEE Int. Freq. Control Symp.*, Newport Beach, CA, June 2–4, 2010, pp. 340–343.

[23] W.-C. Chen, W. Fang, and S.-S. Li, "Quasi-linear frequency tuning for CMOS-MEMS resonators," in *24th IEEE Int. MEMS Conf. Tech. Dig.*, Cancun, Mexico, Jan. 23–27, 2011, pp. 784–787.

[24] K. Wang, A.-C. Wong, and C. T.-C. Nguyen, "VHF free-free beam high-Q micromechanical resonators," *J. Microelectromech. Syst.*, vol. 9, no. 3, pp. 347–360, Sep. 2000.

[25] C.-C. Lo, "CMOS-MEMS resonators for mixer-filter applications," Ph.D. dissertation, Dept. Elect. Comput. Eng., Carnegie Mellon Univ., Pittsburgh, PA, 2008.

[26] J. Verd, M. Sansa, A. Uranga, C. Pey, G. Abadal, F. Perez-Murano, and N. Barniol, "Monolithic CMOS-MEMS oscillators with micro-degree temperature resolution in air conditions," in *15th Int. Conf. Solid-State Sens. Actuators Tech. Dig., TRANSDUCERS*, Denver, CO, Jun. 21–25, 2009, pp. 2429–2432.

[27] W.-L. Huang, "Fully monolithic CMOS nickel micromechanical resonator oscillator for wireless communications," Ph.D. dissertation, Dept. Elect. Eng. Comput. Sci., Univ. Michigan, Ann Arbor, MI, 2008.

[28] M. W. Putty, S. C. Chang, R. T. Howe, A. L. Robinson, and K. D. Wise, "One-port active polysilicon resonant microstructures," in *IEEE Microelectromech. Syst. Workshop Dig.*, Salt Lake City, UT, Feb. 20–22, 1989, pp. 60–65.

Wen-Chien Chen (S'08) received the B.S. degree in mechanical and mechatronic engineering from National Taiwan Ocean University, Keelung, Taiwan, in 2006, and the M.S. degree in power mechanical engineering from National Tsing Hua University, Hsinchu, Taiwan, in 2008, where he is currently working toward the Ph.D. degree.

From 2006 to 2008, his research included the design and fabrication of MEMS resonators for micro-optical scanner applications. From 2008 to date, his doctoral work focuses on temperature stability, mechanical frequency tuning, and Q improvement of integrated micromechanical resonators using CMOS-MEMS technology for RF and sensor applications.

Mr. Chen was the recipient of the Best Student Paper Award at the 14th Conference on NanoEngineering and Microsystems in Taiwan in 2011. Together with his advisor and junior mate, he received the Best Student Paper Award at the 2011 Joint Conference of the IEEE International Frequency Control Symposium and the European Frequency and Time Forum.

Weileun Fang (M'06–SM'11) was born in Taipei, Taiwan. He received the Ph.D. degree from Carnegie Mellon University, Pittsburgh, PA, in 1995.

His doctoral research focused on the determination of the mechanical properties of thin films using micromachined structures. In 1995, he worked as a Postdoctoral Research with the National Synchrotron Radiation Research Center, Hsinchu, Taiwan. He joined the Power Mechanical Engineering Department at National Tsing Hua University, Hsinchu, in 1996, where he is currently a Professor as well as a faculty member of the NEMS Institute. In 1999, he was with Prof. Y.-C. Tai at the California Institute of Technology, Pasadena, as a Visiting Associate. Moreover, he also serves as a technical consultant for many MEMS companies in Taiwan. His research interests include MEMS with emphasis on microfabrication/packaging technologies, CMOS MEMS, CNT MEMS, micro-optical systems, microsensors and actuators, and characterization of thin-film mechanical properties.

Dr. Fang is currently an Editorial Board Member of the *Journal of Micromechanics and Microengineering* (JMM) and an Associate Editor of the IEEE SENSORS JOURNAL and *Journal of Micro/Nanolithography, MEMS, and MOEMS* (JM3). He has served as the chief delegate of Taiwan to the World Micromachine Summit since 2008. He also served on the Technical Program Committee (TPC) of IEEE MEMS'04, MEMS'07, and MEMS'10, the regional TPC of Transducers'07, and the Executive Program Committee of Transducers'09 and Transducers'11. He has been a member of the international steering committee of Transducers since 2009.

Sheng-Shian Li (S'04–M'07) received the B.S. and M.S. degrees in mechanical engineering from National Taiwan University, Taipei, Taiwan, in 1996 and 1998, respectively, and the M.S. and Ph.D. degrees in electrical engineering and computer science from the University of Michigan, Ann Arbor, in 2004 and 2007, respectively.

In 2007, he joined RF Micro Devices, Greensboro, NC, where he was an R&D Senior Design Engineer until mid-2008 for the development of MEMS resonators and filters. In 2008, he joined the Institute of NanoEngineering and MicroSystems at National Tsing Hua University, Hsinchu, Taiwan, where he is currently an Assistant Professor. His research interests focus on nano/microelectromechanical systems, integrated resonators and sensors, RF MEMS, CMOS-MEMS technology, front-end communication architectures, and integrated circuit design and technology.

Dr. Li was the recipient of the Teaching Excellence Award from the College of Engineering, National Tsing Hua University, in 2011. Together with his students, he received the Best Student Paper Award at the 2011 Joint Conference of the IEEE International Frequency Control Symposium and European Frequency and Time Forum.